Acta Materialia 281 (2024) 120428

Contents lists available at ScienceDirect

Acta Materialia

journal homepage: www.elsevier.com/locate/actamat

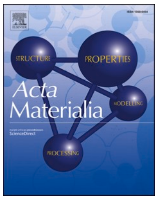

Dislocation-mediated room-temperature mechanical behavior of multiphase entropy stabilized oxides

Salma A. El-Azab [a], Jacob E. Norman [a,b], Luz Gomez [a], Alexander D. Dupuy [a,c], Julie M. Schoenung [a,b,d,*]

[a] *Department of Materials Science and Engineering, University of California, Irvine, CA 92697, United States*
[b] *Department of Materials Science and Engineering, Texas A&M University, College Station, TX 77840, United States*
[c] *Materials Science and Engineering, University of Connecticut, Storrs, CT 06269, United States*
[d] *J. Mike Walker '66 Department of Mechanical Engineering, Texas A&M University, College Station, TX 77840, United States*

ARTICLE INFO

Keywords:
Precipitation strengthening
Dislocations
Mechanical behavior
Ceramics
Entropy stabilized oxides

ABSTRACT

Entropy stabilized oxides (ESOs) exhibit a reversible entropic transformation, which can lead to the formation of secondary phases and tunable microstructures. To date, the interplay between the secondary phases and the mechanical behavior in ESOs has not been explored. In this study, the influence of these secondary phases on the mechanical behavior of the (CoCuMgNiZn)O transition metal ESO (TM-ESO) is investigated. TM-ESOs of equimolar, Co-deficient, and Cu-deficient compositions were fabricated, heat treated to form secondary phases, and characterized. Room-temperature indentation was used to measure the hardness and elastic modulus of single-phase and multiphase bulk samples. Hardness values ranged from 3700 to 6400 MPa, and elastic modulus values ranged from 140 to 170 GPa. As the atomic fraction of secondary phase increases, equimolar and Co-deficient TM-ESO harden then soften, and Cu-deficient TM-ESO continuously hardens. Hardness trends were analyzed by evaluating strengthening mechanisms, indicating that hardness is influenced by the interactions between dislocations and secondary phases. The elastic modulus varies as a function of composition and quantity of secondary phases but falls within a range of values predicted by a composite model. Changing composition influences the hardness and elastic modulus of single-phase TM-ESOs due to changes in cation-dislocation and cation-cation interaction energies. Overall, our findings indicate that the room-temperature mechanical behavior of single-phase and multiphase TM-ESOs is influenced by solid-solution and precipitation strengthening mechanisms, respectively, due to significant dislocation activity. These results demonstrate that the entropic phase transformation can be used to engineer microstructure and tailor the mechanical behavior of ESO materials.

1.0. Introduction

As technological needs advance, conventional methods of developing new, suitable materials are falling short [1]. One creative solution was discovered in 2004, when two groups independently developed high entropy alloys (HEAs), which are composed of five or more elements in approximately equimolar concentrations, and are stabilized by high configurational entropy to form single-phase random solid solutions [2,3]. In 2015, Rost et al. introduced entropy stabilized oxides (ESOs), a novel class of mixed oxide ceramics composed of five or more constituent oxides in equimolar ratios. The composition explored in their study was the (CoCuMgNiZn)O transition metal ESO (hereafter referred to as TM-ESO), which takes on a single-phase rocksalt structure after appropriate processing [4]. One notable finding was that ESOs exhibit a reversible phase transformation. For example, TM-ESO can be taken from its single-phase rocksalt state to a multiphase state, and back to a single-phase state through heat treatment [4].

In 2019, Dupuy et al. demonstrated that the reversible phase transformation in TM-ESOs is influenced by heat treatment conditions [5]. Dupuy et al. varied the heat treatment time and temperature of TM-ESOs and used X-ray diffraction (XRD) to explore the evolution of the secondary phases. Rietveld refinement was used to quantitatively analyze XRD data to estimate the amount of secondary phase that formed for each heat treatment condition. Their results indicated that the secondary phases form in a temperature window of 650 – 850 °C, with the amount of secondary phase being maximized at a heat treatment

---

* Corresponding author.
E-mail address: schoenung@tamu.edu (J.M. Schoenung).

https://doi.org/10.1016/j.actamat.2024.120428
Received 5 April 2024; Received in revised form 20 August 2024; Accepted 22 September 2024

temperature of 700 °C [6]. Using energy dispersive spectroscopy (EDS), Dupuy et al. demonstrated that the secondary phases that form during heat treatment are a Cu-rich tenorite phase and a Co-rich spinel phase, which coexist with the primary rocksalt phase [5]. Dupuy et al. also determined that the primary rocksalt phase retained the stoichiometric distribution of cations without significant depletion of Cu or Co, and the Cu-rich tenorite and Co-rich spinel secondary phases are also multicomponent yet enriched in Cu and Co, respectively [7]. Thus, the configurational entropy is retained in the primary rocksalt phase.

Although the field of entropy stabilized ceramics has rapidly expanded in recent years, an examination of the literature shows only a few studies investigating the mechanical behavior of TM-ESOs, and all are focused on single-phase TM-ESOs. For instance, Braun et al. used atomic force microscopy (AFM) on single-phase TM-ESO thin films and determined that the elastic modulus was 152.0 ± 10.6 GPa [8]. Pitike et al. used density functional theory (DFT) and nanoindentation to determine that single-phase TM-ESOs exhibit mechanical anisotropy due to local structure and magnetic configuration and that the elastic modulus ranges from 212 to 228 GPa [9]. Hong et al. varied the sintering temperature of single-phase TM-ESOs in 50 °C increments from 800 °C to 1000 °C, and measured the grain size, relative density, bending strength, and elastic modulus of as-sintered samples. They reported that grain size and relative density increase with increasing sintering temperature, but that bending strength and elastic modulus peak at a sintering temperature of 900 °C, having values of 323 ± 19 MPa and 108 ± 5 GPa, respectively [10]. Wang *et al.* investigated the room-temperature mechanical deformation of single-phase TM-ESOs using nano-scratch tests, and found a high level of dislocation activity in the region of deformation [11].

Notably, the influence of the entropic phase transformation on the mechanical behavior of TM-ESOs, including hardness and elastic modulus, remains unexplored. Additionally, little is understood about how the presence of dislocations and their interactions with secondary phase particles influences the mechanical response in multiphase TM-ESOs. Previous studies on other multiphase ceramics demonstrate that secondary phases can influence their mechanical behavior. For example, Mayrhofer et al. reported an increase in hardness in heat-treated $Ti_{1-x}Al_xN$ ceramics due to the formation of a two-phase microstructure from spinodal decomposition [12]. Spinodal decomposition of yttria-stabilized zirconia (YSZ) also results in an increase in hardness [13]. Additionally, recent developments in the area of high entropy oxide composites (HEOCs) have shown that the addition of a secondary phase influences their mechanical properties. Zhong et al. demonstrated that $Al_2O_3/(Y_{0.2}Er_{0.2}Yb_{0.2}Ho_{0.2}Lu_{0.2})_3Al_5O_{12}$ eutectic ceramic composites with and without ZrO_2 exhibit high fracture toughness due to composite strengthening mechanisms such as crack bridging, bifurcation, deflection, and screening [14,15]. Tu *et al.* observed that rare earth aluminate HEOCs exhibit high fracture toughness values due to the addition of a secondary phase leading to a particulate strengthening effect [16]. Feng *et al.* observed that rare earth-based HEOCs with equiaxed dendritic microstructures exhibit high fracture toughness values due to high thermal expansion mismatch between the different phases [17]. These previous studies demonstrate that HEO materials provide significant design space for engineering mechanical behavior.

The above-described studies focus on composite and particulate toughening mechanisms, where the microstructural features are on the order of tens of microns. Our previous studies demonstrate that entropic transformations in TM-ESO can generate secondary phases with morphology length-scales that are < 1 μm [5,7,18]. Given recent investigations into the entropic phase transformations in TM-ESOs [5,7], the known influence of secondary phases on the mechanical response of ceramics [12,13], and recent developments in HEOCs [14–17] as described above, the current investigation aims to develop an understanding of how hardness and elastic modulus are influenced by the presence of secondary phases within multiphase TM-ESOs, using well-known precipitation mechanisms and a composite model as the basis for the analysis of mechanical response. TM-ESOs of various compositions were fabricated and heat treated at different time increments to form different quantities of secondary phases. The phase transformation was characterized using scanning electron microscopy (SEM), EDS, and XRD. Room-temperature Vickers hardness testing and nanoindentation were used to measure the hardness and elastic modulus, respectively, for each processing condition. Scanning transmission electron microscopy (STEM) was used to analyze the interactions between dislocations and secondary phase particles inside and outside of the deformation region. Mechanisms that lead to the observed variations in hardness and elastic modulus were evaluated.

2.0. Methods

2.1. Selection of material composition

Three different TM-ESO compositions were selected: equimolar TM-ESO (CoCuMgNiZn)O), a Co-deficient composition with the chemical formula of $(CuMgNiZn)_{0.9}Co_{0.1}O$, and a Cu-deficient composition with a formula of $(CoMgNiZn)_{0.9}Cu_{0.1}O$. We hypothesize that by introducing a deficiency of Co and Cu, we can isolate the Cu-rich tenorite and Co-rich spinel secondary phases, respectively, to analyze their role on the mechanical behavior independently. The predicted theoretical densities and predicted secondary phases for each TM-ESO composition are provided in Table 1.

2.2. Powder preparation and fabrication of ESOs

TM-ESO powders for each composition were prepared through solid-state synthesis. A powder blend of constituent oxides was created from CoO, CuO, MgO, NiO, and ZnO oxide nanopowders (50 nm, 25 – 55 nm, 50 nm, 18 nm, 18 nm, respectively), which were all at least 99.7 % pure (US Research Nanomaterials, Houston, TX, USA). These five oxide powders were blended with a mortar and pestle, then placed in a Si_3N_4 planetary ball mill (PBM) jar with isopropyl alcohol and milled for 3 h at 300 RPM in a Pulverisette 7 PBM instrument (Fritsch, Idar-Oberstein, Germany). The powder slurries were extracted from the PBM jar and boiled at 100 °C for 12 h to evaporate the isopropyl alcohol. The dried powder was ground in a mortar and pestle to remove agglomerates. Bulk samples of each composition were consolidated using conventional sintering. Compacted green bodies were placed in an elevator furnace (CM Furnaces Inc. Bloomfield, NJ, USA) and conventionally sintered at 1100 °C for 12 h to form fully dense, single-phase samples. After 12 h, the samples were quenched in air to preserve the single-phase state.

The density of the as-sintered single-phase samples was measured using the Archimedes method [19] and compared to the theoretical density values provided in Table 1. Fracture surfaces were prepared for SEM analysis by sputter coating with 3 nm of iridium using an ACE600 sputter coating machine (Leica Microsystems, Wetzlar, Germany). The fracture surfaces were imaged with a Magellan 400 XHR SEM (FEI, Hillsboro, OR, USA), using an accelerating voltage of 5 kV and a current of 50 pA. The average grain size was calculated from the fracture surface micrographs by measuring the diameter of approximately 500 grains with the FIJI/ImageJ software [20].

Table 1
Calculated theoretical densities and predicted secondary phases for each composition of TM-ESO.

TM-ESO Composition	Chemical Formula	Theoretical Density (g/cm^3)	Predicted Secondary Phases
Equimolar	(CoCuMgNiZn)O	5.70	Cu-rich tenorite, Co-rich spinel
Co-deficient	$(CuMgNiZn)_{0.9}Co_{0.1}O$	5.61	Cu-rich tenorite
Cu-deficient	$(CoMgNiZn)_{0.9}Cu_{0.1}O$	5.67	Co-rich spinel

2.3. Heat treatment and characterization of secondary phases

Previous work has demonstrated that heat treatments within a particular temperature window can stimulate the formation of secondary phases in TM-ESO [5]. In the current study, the single-phase samples were heat treated in the elevator furnace for either 2 or 12 h to form secondary phases, to study the overall effect of secondary phase concentration on the mechanical behavior of TM-ESO. These heat treatment times were determined on the basis of a previous publication in which secondary phase formation as a function of time and temperature were studied in detail [5]. The equimolar and Co-deficient compositions were heat treated at 700 °C, and the Cu-deficient composition was heat treated at 600 °C. For each composition, these temperatures were found to be the ones at which the most secondary phase forms upon heat treatment. The samples were air quenched at the end of each heat treatment. The bulk samples were polished with 800 grit and 1200 grit SiC pads (Allied High-Tech Products, Inc., Compton, CA, USA), then with 6 μm and 1 μm diamond suspensions (PACE Technologies, Tucson, AZ, USA). XRD analysis was conducted with a SmartLab X-ray Diffractometer (Rigaku, Tokyo, Japan), at a 2θ range of 30° to 80° Rietveld refinement was performed on the acquired XRD data using the Maud software [21] to estimate the relative atomic fractions of the primary rocksalt, Cu-rich tenorite, and Co-rich spinel phases for each heat treatment condition for the three compositions.

The polished equimolar and Co-deficient samples were mounted onto SEM stubs with colloidal silver paste (Ted Pella Inc., Redding, CA, USA) and sputter coated with 3 nm of iridium. EDS was performed in a GAIA3 SEM-FIB microscope (Tescan, Brno, Czechia) using a silicon drift detector with an area of 150 mm^2 (Oxford Instruments, Abingdon, UK). A working distance of 5 mm and an accelerating voltage of 5 kV were used. Our previous work has demonstrated that performing EDS with low accelerating voltages is useful for resolving the fine secondary phase features found in TM-ESO [5].

2.4. Room-temperature Vickers hardness testing

Vickers hardness indentation experiments were performed at room temperature on single-phase and multiphase samples. Samples were first mounted in Konductomet mounting media (Buehler, Lake Bluff, IL, USA) and polished down to a 1 μm finish. Vickers hardness indentation measurements were done with a Wilson VH3300 indenter (Buehler, Lake Bluff, IL, USA) with a load of 100 g and a dwell time of 10 s. Fifteen measurements were taken per sample. Depth profiles from corner to corner for each indent were collected with a LEXTTM OLS5100 3D Laser Scanning Microscope (Olympus, Tokyo, Japan) to get accurate measurements of indent dimensions to estimate hardness values. Indent dimensions were used to determine the Vickers hardness values, H, for each sample using the following equation [22]:

$$H = 1.854\frac{F}{(2a)^2} \tag{1}$$

where F is the load (kg) and a is the indent half diagonal (mm).

Electron transparent lamella samples were prepared for STEM experiments using focused ion beam (FIB) milling. Lamella samples were prepared using FIB lift-out techniques from two regions of an equimolar sample that was heat treated for 12 h at 700 °C: both inside and outside the plastic deformation zone created by the Vickers hardness indentation. The lamella samples were each 10 μm long, 5 μm wide, and 100 nm thick. The lamella sample from inside the plastic deformation zone was lifted out from underneath the Vickers indent, along its diagonal. The lamella sample from outside the deformation zone was lifted from a region of the sample far from the cluster of indents to ensure that it was not affected by the deformation zone below the indents, a distance more than 10 times the size of the indent [23,24]. A JEOL 2800 TEM/STEM (JEOL Ltd., Tokyo, Japan) was used at 200 kV with a Gatan OneView Camera (AMETEK, Berwyn, PA, USA) to observe dislocations and secondary phase morphology.

2.5. Room-temperature nanoindentation

Nanoindentation experiments were performed at room temperature with a Hysitron PI-85 system (Bruker, Billerica, MA, USA) to measure elastic modulus. Samples were first polished to a 1 μm finish and mounted to a sample holder with silver paste. A Berkovich tip was used to apply a load of 5 mN at a load rate of 1 mN/s and a hold time of 2 s. Fifty measurements were taken per sample, and elastic modulus values were calculated by a proprietary Bruker software.

3.0. Results

The as-sintered samples had a relative density of 99 %. Representative micrographs depicting the microstructure of the three different compositions in their as-sintered state are displayed in Fig. 1. The grains take on an equiaxed structure in all compositions. The equimolar TM-ESO has the largest grain size (12.1 ± 4.8 μm), followed by the Co-deficient TM-ESO (7.6 ± 3.1 μm), and the Cu-deficient TM-ESO (4.0 ± 1.3 μm).

XRD results are shown in Fig. 2. For all three compositions, the XRD spectra corresponding to the as-sintered state (0 h heat treatment, shown in black) indicate a single-phase rocksalt structure, with no sign of any extraneous peaks or secondary phases. After 2 h of heat treatment, peaks corresponding to Cu-rich tenorite and Co-rich spinel secondary phases appear for the equimolar composition. For the Co-deficient composition, peaks corresponding to the Cu-rich tenorite appear. The Cu-deficient composition remained in a single-phase state. As the heat treatment time increases to 12 h, the peaks corresponding to the secondary phases become more prominent for the equimolar and Co-deficient compositions, indicating that the secondary phases increased in concentration. Peaks corresponding to the Co-rich spinel phase appear for the Cu-deficient composition after 12 h of heat treatment.

Rietveld refinement results for quantification of the atomic fraction (at %) of secondary phases are summarized in Table 2. For the equimolar composition, after 2 h of heat treatment, there is an equal amount of the Co-rich spinel and Cu-rich tenorite secondary phases (6 at % each). After 12 h of heat treatment, there is more Cu-rich tenorite (14 at %) than Co-rich spinel (10 at %). For the Co-deficient composition, as the heat treatment time increases from 2 to 12 h, the concentration of Cu-rich tenorite increases from approximately 5 at % to 16 at %. For the Cu-deficient compositions, after 12 h of heat treatment, there is 8 at % Co-rich spinel.

Secondary electron (SE) images and corresponding composition maps captured through EDS are shown in Fig. 3 for the equimolar and Co-deficient compositions. For further characterization of these secondary phase particles, the readers are also referred to several previous studies by Dupuy *et al.* [5,7,18]. For the equimolar sample, the Cu-rich tenorite particles take on a needle-like morphology after 2 h of heat treatment, as shown in Fig. 3a & b. The Co-rich spinel particles are small and difficult to resolve using EDS, as shown in Fig. 3c. After 12 h of heat treatment, these Cu-rich particles coarsen and adopt a slight curvature, shown in Fig. 3d & e. The Co-rich spinel particles also coarsen and adopt a spherical morphology, as shown in Fig. 3f. In the Co-deficient composition, after 2 h of heat treatment, the Cu-rich needles are well-formed, straight, and more elongated than the equimolar composition, as shown in Fig. 3g & h. After 12 h of heat treatment, the Cu-rich needles coarsen, but maintain their straight morphology, shown in Fig. 3i & j. The micrographs of the Cu-rich tenorite particles were used to determine their variations in size and spacing as the heat treatment time increases. Since EDS is not sufficient to provide such quantitative values for the Co-rich spinel particles, the results from the extensive atom probe tomography and FIB-tomography studies by Dupuy *et al.* are used instead [7,18].

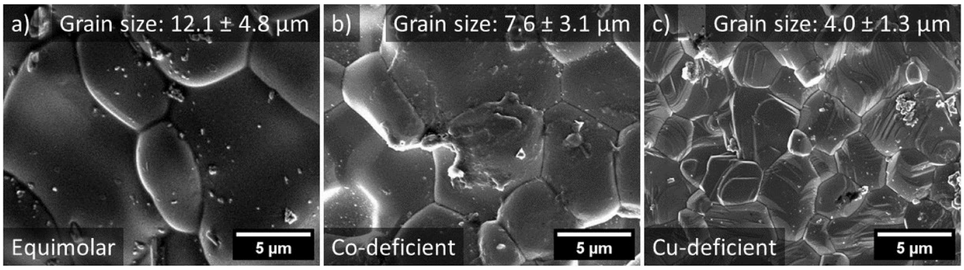

Fig. 1. Fracture surfaces of as-sintered TM-ESO with: a) equimolar composition, b) Co-deficient composition, and c) Cu-deficient composition. The small particles are debris remaining from the fracture process. Average grain size values are provided for each.

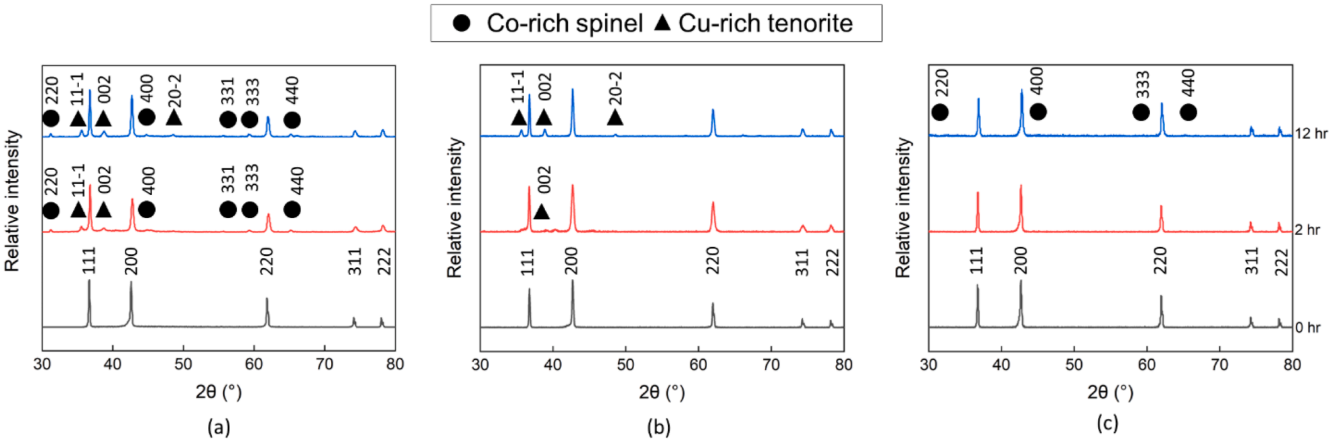

Fig. 2. XRD spectra showing the phase evolution for TM-ESO heat treated for 0, 2, and 12 h time intervals; a) equimolar composition, b) Co-deficient composition, and c) Cu-deficient composition. The as-sintered samples are single phase, and the heat-treated samples are multiphase.

Table 2

Concentration of primary (rocksalt) and secondary (Cu-rich tenorite and Co-rich spinel) phases as a function of heat treatment time and TM-ESO composition.

TM-ESO Composition	Heat Treatment Time (h)	Rocksalt (at %)	Cu-rich Tenorite (at %)	Co-rich Spinel (at %)
Equimolar	0	100	0	0
	2	88	6	6
	12	76	14	10
Co-deficient	0	100	0	0
	2	95	5	0
	12	84	16	0
Cu-deficient	0	100	0	0
	2	100	0	0
	12	92	0	8

Vickers hardness test results are shown in Fig. 4. Values range from 3700 ± 120 MPa to 6400 ± 190 MPa, depending on composition and heat treatment conditions. For the equimolar and Co-deficient composition, the hardness initially increases from the as-sintered single-phase state to the 2 h heat-treated state. After 12 h of heat treatment, the hardness decreases. For the equimolar composition, the hardness decreases until it is lower than it was in the single-phase state. For the Co-deficient composition, the hardness decreases until it reaches a level very similar to its single-phase state. The hardness test results for the equimolar and Co-deficient TM-ESO compositions indicate that as the amount of secondary phase increases, the TM-ESO hardens then softens. The Cu-deficient composition continuously increases in hardness as heat treatment time increases and the secondary phase starts to form. In addition to the influence of heat treatment time, composition also plays a role in hardness. The Co-deficient composition has the highest overall hardness, and the Cu-deficient composition has the lowest overall hardness, regardless of heat treatment condition.

Fig. 5 shows dislocation activity in an equimolar TM-ESO sample that was heat treated for 12 h. A TEM bright field micrograph of a region outside of the plastic deformation zone (i.e., away from the Vickers indent) is shown in Fig. 5a. The dark regions are Cu-rich tenorite secondary phase particles. In this region, there is little to no dislocation activity outside of the plastic deformation zone, indicating that TM-ESO does not have a meaningful concentration of dislocations prior to deformation. Fig. 5b shows a STEM dark field micrograph taken from directly underneath the indent. The bright regions are the Cu-rich tenorite secondary phase particles, and the dark regions are dislocation clouds. After deformation, there is significant dislocation activity in the deformation zone. Additionally, the dislocations pile up near the Cu-rich tenorite particles, indicating that they interact directly with these secondary phase particles.

Nanoindentation was performed to acquire elastic modulus values. No noticeable pop-in effects were observed in the load vs. displacement curves for each heat treatment condition across all compositions (see Figure S1 in the Supplementary Material). The results from elastic modulus measurements are shown in Fig. 6. Values range from 140 ± 5 GPa to 170 ± 6 GPa, depending on composition and heat treatment conditions. The elastic modulus for the equimolar composition increases as heat treatment time increases and more secondary phases form. For the Co-deficient and Cu-deficient compositions, the elastic modulus varies with the secondary phase composition.

4.0. Discussion

4.1. Room-temperature hardness trends in multiphase TM-ESO

Mechanical properties such as hardness and strength are influenced by several mechanisms, such as dislocation activity. Dislocation activity

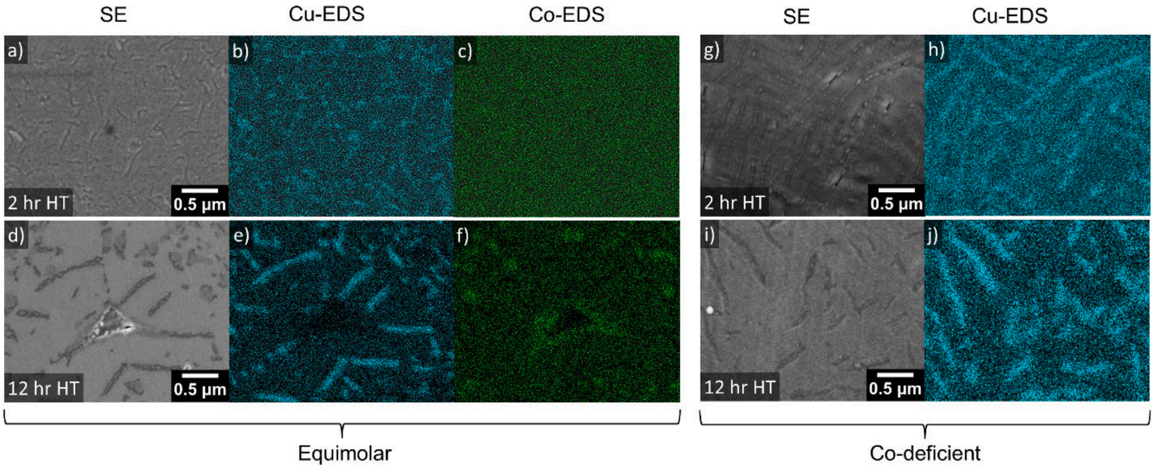

Fig. 3. Secondary electron (SE) SEM and corresponding Cu-EDS and Co-EDS maps of Cu-rich tenorite and Co-rich spinel phases in (a) – (c) equimolar, 2 h heat treatment; (d) – (f) equimolar, 12 h heat treatment; SEM and corresponding Cu-EDS maps of Cu-rich tenorite phases in (g) – (h) Co-deficient, 2 h heat treatment; (i) – (j) Co-deficient, 12 h heat treatment. HT refers to heat treatment.

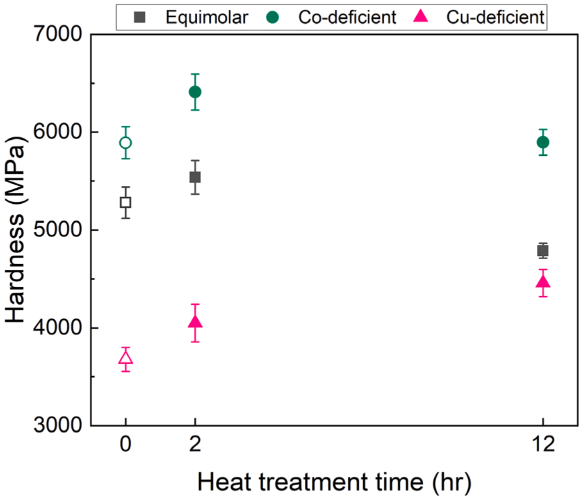

Fig. 4. Room-temperature Vickers hardness results for equimolar, Co-deficient, and Cu-deficient TM-ESOs: as-sintered, heat treated for 2 h, and heat treated for 12 hr. The as-sintered samples are single-phase (represented by the open symbols at 0 hr), and the heat-treated samples are multiphase (represented by closed symbols at 2 h and 12 h), as summarized in Table 2.

is not typically prescribed as a dominant influence in the deformation behavior of ceramics, which are more likely to deform in a brittle manner, as their slip systems are difficult to activate [25]. Notably, unusually high dislocation activity has been previously observed in ESOs [11,26]. Additionally, a recent study by Vahidi et al. demonstrates through high-resolution TEM imaging that semi-coherent interfaces between Cu-rich tenorite secondary phase particles and the surrounding rocksalt primary phase in TM-ESO result in misfit strain that is accommodated by edge dislocations [27]. The TEM micrographs in Fig. 5 show that dislocations are present in the deformation region but are not observed outside of that region, indicating that the dislocations are not intrinsic to the TM-ESO but were introduced during the room-temperature indentation experiments. Additionally, Fig. 5b shows that dislocations interact directly with secondary phase particles. Based on the previous literature and our observations of dislocation activity in this investigation, we hypothesize that dislocations play a significant role in the room-temperature mechanical behavior of TM-ESOs. As such, the ensuing discussion is interpreted through the lens of classical dislocation phenomena, more specifically, precipitation strengthening.

Precipitation strengthening accounts for several strengthening mechanisms caused by the interactions of moving dislocations with precipitates or secondary phase particles [28]. Precipitation strengthening is commonly observed in metals, where slip systems are readily activated and dislocations move easily [25]. Notably, precipitation strengthening has also been observed in ceramic systems, such as $MgAl_2O_4$ spinel [29]. Precipitation strengthening mechanisms can be categorized depending on how moving dislocations interact with secondary phase particles [30,31]. The first category is by shearing, where dislocations directly cut through the particle. Shearing mechanisms typically dominate when particles are small and coherent with their surroundings (e.g., early-stage precipitation). The second category is bypassing, where dislocations pass the particle rather than shear directly through. Bypassing mechanisms typically dominate when the size of the secondary phase particle exceeds a critical value (e.g., late-stage precipitation) or when particles are incoherent with their surroundings. Shearing and bypassing mechanisms occur simultaneously and independently of each other. Additionally, each mechanism contributes a specific strengthening increment. Whichever mechanism has the smallest strengthening increment value is the mechanism that is easiest to activate, meaning that this “softer” mechanism initiates and controls plastic deformation [30,31].

To explore the potential strengthening mechanisms in multiphase TM-ESO materials, three specific hardening mechanisms are evaluated: coherency hardening, modulus hardening, and Orowan hardening. Coherency hardening and modulus hardening are shearing mechanisms, while Orowan hardening is a bypassing mechanism. Coherency hardening occurs when the coherency of the secondary phase particles with the primary phase leads to internal lattice strain, resulting in associated stress fields that draw or repel dislocations to or away from the particle [28]. The value of the strengthening increment, τ_{coh}, due to coherency hardening can be estimated with the following equation [28]:

$$\tau_{coh} \cong 7|\varepsilon_{coh}|^{3/2} G \left(\frac{rf}{b}\right)^{1/2} \tag{2}$$

where r is the secondary phase particle radius, f is the volume fraction of particles, G is the shear modulus of the secondary phase particle, and b is the magnitude of the Burger’s vector in the primary phase (the rocksalt phase). ε_{coh} can be expressed by the following equation [28]:

$$\varepsilon_{coh} = \frac{a_p - a_m}{a_m} \tag{3}$$

where a_p is the lattice parameter of the secondary phase particle and a_m

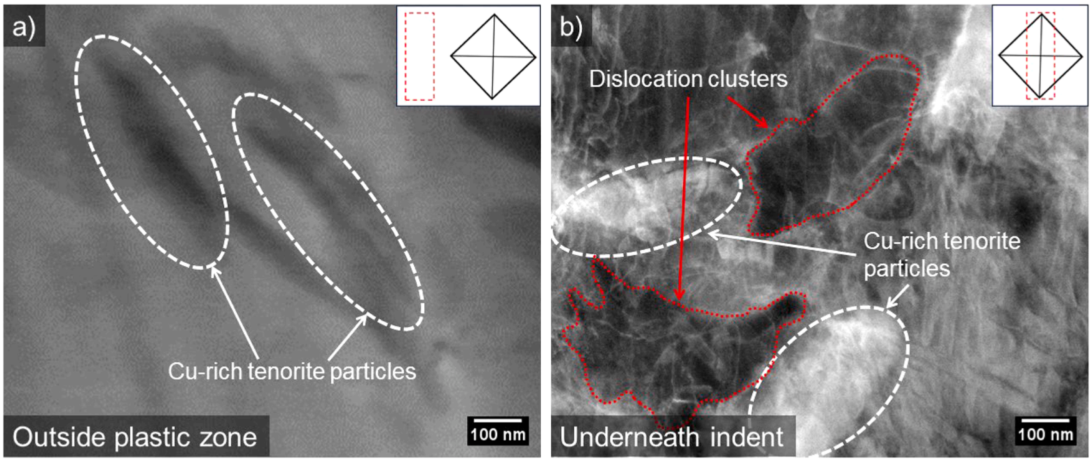

Fig. 5. TEM micrographs taken from an equimolar TM-ESO sample that was heat treated at 700 °C for 12 h showing: a) A TEM bright field image from outside the plastic deformation zone far from the Vickers indents, and b) a STEM dark field micrograph from inside the plastic deformation zone located underneath the Vickers indent. Cu-rich tenorite secondary phase particles are highlighted in white and dislocation clusters are highlighted in red. The inset schematics indicate the location of the lift-outs relative to the indent (note: these are not to scale).

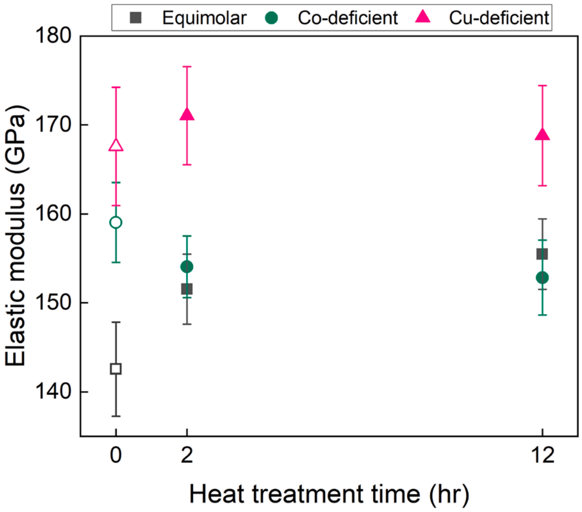

Fig. 6. Room-temperature elastic modulus results for the equimolar, Co-deficient, and Cu-deficient TM-ESO after heat treating for 0 h, 2 h, and 12 h. As-sintered samples are single phase (represented by open symbols at 0 h), and heat-treated samples are multiphase (represented by closed symbols at 2 h and 12 h), as summarized in Table 2.

is the lattice parameter of the surrounding primary phase.

Modulus hardening occurs when a dislocation enters a secondary phase particle that has a different shear modulus than that of the surrounding primary phase, altering the dislocation line tension [28]. The strengthening increment, τ_{Gp}, caused by modulus hardening can be estimated with the following equation [28]:

$$\tau_{Gp} \cong 0.01 G \varepsilon_{Gp}^{3/2} \left(\frac{rf}{b}\right)^{1/2} \tag{4}$$

ε_{Gp} can be expressed with the following equation:

$$\varepsilon_{Gp} = \frac{G - G_m}{G_m} \tag{5}$$

where G_m is the shear modulus of the surrounding primary phase.

Orowan hardening occurs when a dislocation approaches a secondary phase particle, bows around it, and forms a loop before eventually continuing through the primary phase [28]. The strengthening increment, τ_B, due to Orowan hardening can be estimated with the following equation [28]:

$$\tau_B \cong \frac{Gb}{(L - 2r)} \tag{6}$$

where L is the mean spacing between secondary phase particles.

Estimated results for coherency hardening, modulus hardening, and Orowan hardening strengthening increments are listed in Table 3. Values for f, b, a_m, and a_p were collected from XRD data (see Fig. 2 and Table 2). Values for r and L for the Cu-rich tenorite secondary phase particles were approximated from SEM and EDS images (see Fig. 3). Values for r and L for the Co-rich spinel phase were approximated from the literature [7,18]. Shear modulus data for the secondary phases were collected from the literature [9,32]. All values used for these calculations are tabulated in Tables S3-S5 in the Supplementary Materials.

As shown in Table 3, the equimolar samples experience a change in the operative hardening mechanism from modulus hardening (with a strengthening increment of 0.1 GPa) after 2 h of heat treatment to Orowan hardening (with a strengthening increment of 0.1 GPa) after 12 h of heat treatment. Similarly, the Co-deficient samples experience a transition from modulus hardening (with a strengthening increment of 0.081 GPa) after 2 h of heat treatment to Orowan hardening (with a strengthening increment of 0.078 GPa) after 12 h of heat treatment. Notably, for both compositions, coherency hardening is not the operative strengthening mechanism, despite the previously observed misfit strain at the interfaces between the Cu-rich tenorite needles and the primary rocksalt phase [27]. As shown in Fig. 4, the equimolar and Co-deficient compositions initially harden after 2 h of heat treatment,

Table 3
Estimated strengthening increment values for coherency hardening, modulus hardening, and Orowan hardening for multiphase equimolar, Co-deficient, and Cu-deficient TM-ESO. The bolded values represent the operative mechanism, which has the smallest strengthening increment value.

TM-ESO Composition	Heat Treatment Time (h)	Hardening Mechanism		
		Coherency (GPa)	Modulus (GPa)	Orowan (GPa)
Equimolar	2	8.6	**0.1**	1.8
	12	11.7	0.12	**0.10**
Co-deficient	2	7.2	**0.1**	0.3
	12	7.8	0.081	**0.078**
Cu-deficient	2	**0.01**	0.04	67.8
	12	8.6	**0.1**	1.8

and then soften after 12 h of heat treatment. Such a trend in hardness increasing then decreasing with heat treatment is attributed to a change in the operative hardening mechanism from a shearing mechanism to a bypassing mechanism. As the heat treatment time increases, the secondary phase particles coarsen and the particle spacing increases, as shown in Fig. 3, due to copper diffusion from the primary phase into the Cu-rich tenorite secondary phase, causing it to be more energetically favorable for dislocations to bow around secondary phase particles rather than shear directly through them [28]. Additionally, as the secondary phase particles further coarsen and particle spacing increases with longer heat treatment time, the stress associated with dislocation bowing decreases, meaning that less energy is imparted during bowing [28]. These secondary phase particle coarsening effects are reflected in the observed trends for equimolar and Co-deficient TM-ESOs by the decrease in hardness with longer heat treatment time. Overall, this transition from a shearing mechanism to a bypassing mechanism, and consequential increase and decrease in room-temperature hardness, is similar to hardening trends observed in Ni-Al alloys [28,33] and age-hardened Al-Cu alloys [34,35].

A different trend is observed in the hardness data for the Cu-deficient composition. As shown in Fig. 4, the Cu-deficient samples initially strengthen after 2 h of heat treatment, although no Co-rich spinel formed at this stage according to XRD results shown in Fig. 2. Dupuy et al. has shown that Co-rich spinel and Cu-rich tenorite secondary phases form through the nucleation and growth of nanoparticle precursor phases, and their eventual transition into their respective secondary phases [7]. According to Dupuy et al., these nanoparticle precursor phases have distorted rocksalt lattice structures. Though distorted, these nanoparticle precursor phases are coherent with the primary rocksalt phase, likely contributing to coherency hardening as the operative hardening mechanism with a strengthening increment of 0.01 GPa, as shown in Table 3. This phenomenon is similar to the role of GP-zones in age-hardened Al-Cu alloys, which cause lattice distortions while maintaining coherency with their surroundings, causing hardening to occur at shorter ageing times [34,35]. After 12 h of heat treatment, Co-rich spinel secondary phase particles have formed. Notably, the Cu-deficient samples harden further – they do not soften as is observed for the equimolar and Co-deficient compositions. As shown in Table 3, the change in strengthening increment values from 0.01 GPa for coherency hardening at 2 h heat treatment to 0.1 GPa for modulus hardening at 12 h heat treatment indicates a transition from coherency hardening to modulus hardening. At this stage, the observed increased in hardness is likely due to a change in dislocation line tension as dislocations shear directly through the newly formed Co-rich spinel secondary phase particles, which have a different shear modulus than the surrounding primary rocksalt phase. We propose here that the strengthening trend observed for the Cu-deficient composition is caused by a transition from coherency hardening due to the distortion of the lattice by coherent nanoparticle precursor phases, to modulus hardening upon complete formation of the Co-rich spinel secondary phase particles. The overall hardening trends and associated strengthening mechanisms are summarized in Fig. 7.

4.2. Room-temperature elastic modulus trends in multiphase TM-ESO

Some studies suggest that the elastic modulus of a multiphase material is influenced by the elastic moduli and concentration of the secondary phase particles, if the elastic moduli of secondary phase particles are significantly different than that of the surrounding primary phase [36,37]. This behavior is consistent with conventional composite materials, where an applied load is transferred from a matrix phase to the embedded fibers [38]. The TM-ESO samples in this study were fully dense and had similar microstructures across all compositions (Fig. 1), eliminating density and microstructure as influences on elastic modulus. Additionally, previous experiments by Dupuy et al. show that the primary rocksalt phase retains its configurational entropy after the formation of secondary phases, eliminating any solid solution strengthening effect as an influence on the elastic modulus of multiphase

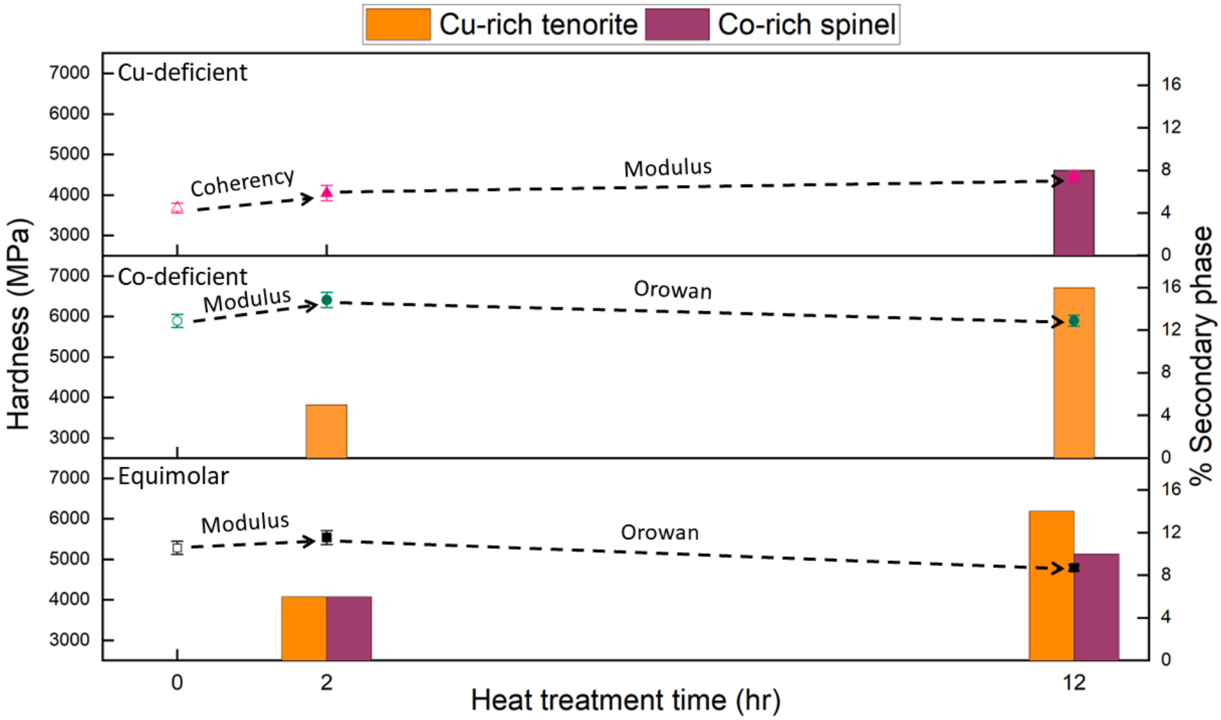

Fig. 7. A schematic summarizing the room-temperature hardening trends observed in equimolar, Co-deficient, and Cu-deficient TM-ESO with increasing amounts of secondary phase due to longer heat treatments and associated strengthening mechanisms. The as-sintered samples are single-phase (as represented by the open symbols at 0 h), and heat-treated samples are multiphase (as represented by the closed symbols at 2 h and 12 h), as summarized in Table 2. The operative hardening mechanism, which has the smallest strengthening increment value, is noted above the dotted lines, accordingly.

TM-ESO [7]. As such, we hypothesize that the variations in elastic modulus observed in this study (Fig. 6) are due to the formation of secondary phases and that the behavior is similar to that of conventional composite materials. Thus, we applied the Voigt model to estimate elastic modulus as a weighted average of the elastic moduli values of the primary rocksalt phase, and the secondary Cu-rich tenorite and Co-rich spinel phases. The Voigt model was selected as it is a simple approximation that can be used to estimate the elastic modulus of a material containing more than two phases. The equation for the Voigt model is [39]:

$$E = \sum v_i \cdot E_n \tag{7}$$

where v_i is the volume fraction of each respective phase, and E_n is the modulus of each respective phase. Lower and upper bound elastic modulus values found in literature for the secondary phases, listed in Table S6, were used to estimate a range of expected elastic modulus values for the equimolar, Co-deficient, and Cu-deficient TM-ESOs. The experimental elastic modulus values are plotted together with this range of expected values estimated with the Voigt model in Fig. 8.

The room-temperature elastic modulus values for all three compositions fall within the range of expected values calculated with the Voigt model, as shown in Fig. 8. While this range of values is not intended to explain the cause for the change in elastic modulus observed experimentally as more secondary phases form, it does provide an indication of how reasonable the experimentally measured values are for the multiphase TM-ESO materials, relative to what has been previously reported in literature for elastic modulus values of CuO tenorite and Co_3O_4 spinel. The room-temperature elastic modulus values for the equimolar and Co-deficient compositions fall approximately in the middle of the expected range. In contrast, the measured values for the Cu-deficient composition skew towards the higher values, indicating that the Co-rich spinel elastic modulus is likely closer to the upper bound elastic modulus value for Co_3O_4 spinel (Table S6).

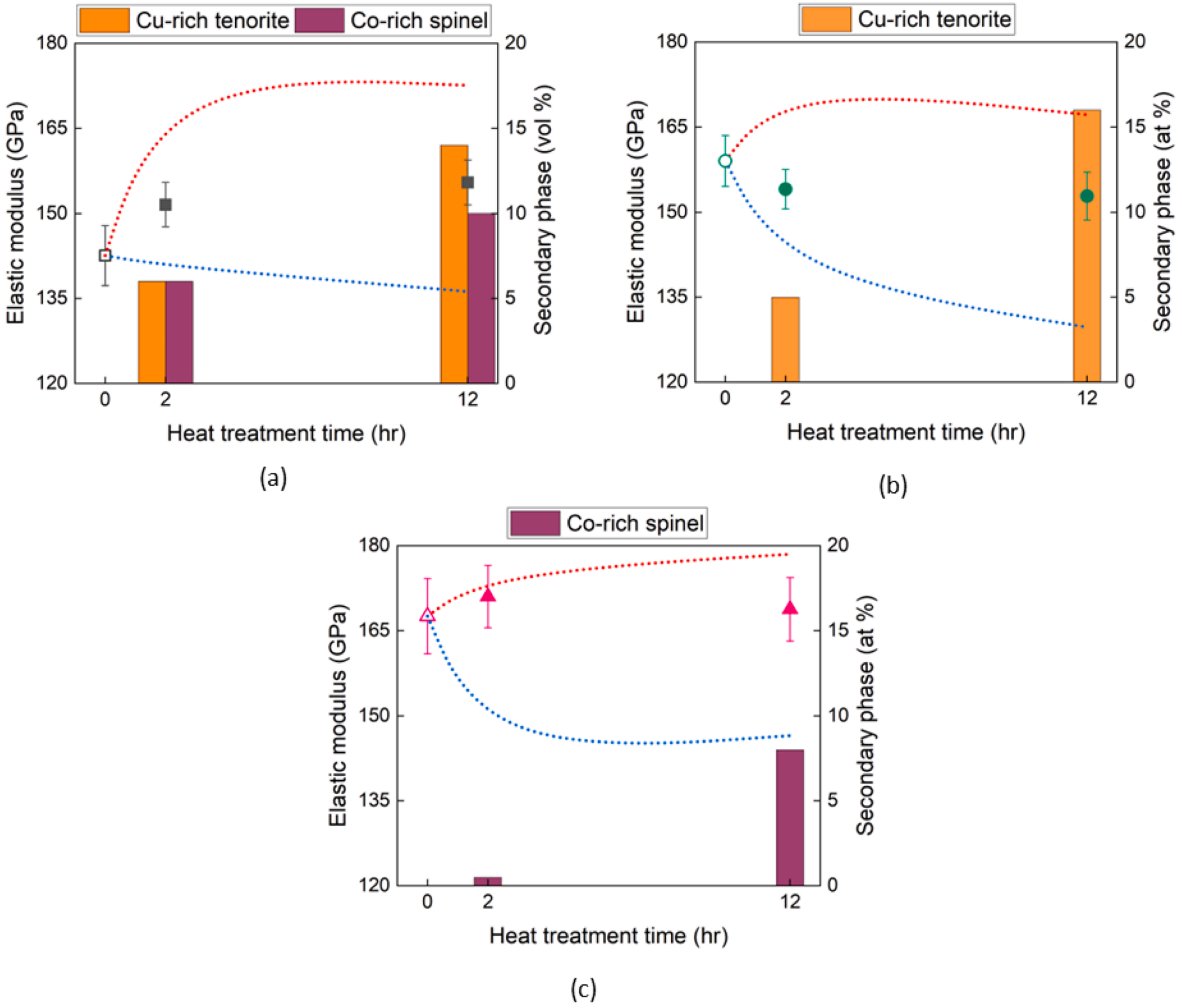

Fig. 8. Graphs showing room-temperature elastic modulus values and where they fall within the range of expected elastic modulus values (red dotted lines and blue dotted lines) for: a) equimolar, b) Co-deficient, and c) Cu-deficient TM-ESO. As-sintered samples are single-phase (as represented by the open symbols at 0 hr), and heat-treated samples are multiphase (as represented by the closed symbols at 2 h and 12 h), as summarized in Table 2. The red dotted lines and blue dotted lines represent the upper and lower bound elastic modulus values, respectively, as predicted by the Voigt model for modulus variation due to the precipitation of secondary phases.

4.3. Influence of composition on room-temperature mechanical behavior of single-phase TM-ESO

Composition significantly influences the overall room-temperature hardness and elastic modulus of the TM-ESO materials in this study, even in the as-sintered single-phase state. As shown in Figs. 4 and 6, the single-phase equimolar, Co-deficient, and Cu-deficient TM-ESOs have room-temperature hardness values of approximately 5300 MPa, 5900 MPa, and 3700 MPa, respectively, and room-temperature elastic modulus values of approximately 140 GPa, 160 GPa, and 170 GPa, respectively. Similar changes in mechanical behavior with changes in composition have also been observed experimentally in HEAs [40,41]. Such changes in mechanical properties are often attributed to changes in lattice distortion and solute configuration with changes in composition [40,41]. As a result, the energy associated with two types of interactions changes: cation-dislocation interactions, and cation-cation interactions, which cause an elastic effect and a chemical effect, respectively [40,41].

The elastic effect refers to changes in the energy associated with cation-dislocation interactions, which influence hardness and strength. As the composition of the TM-ESO changes, the location of cations, relative to dislocations, changes. Thus, the energy needed for a dislocation to travel through the lattice changes accordingly [40], resulting in an effect similar to solid-solution strengthening [28]. To estimate if the variations in hardness caused by changes in composition can be caused by the elastic effect, solid-solution strengthening increment values were calculated using the following equation [31]:

$$\Delta\tau_{ss} = MGB\varepsilon_{ss}^{3/2}\sqrt{c} \qquad (8)$$

where M is the mean orientation factor (3.06 for FCC solids such as the primary rocksalt phase), ε_{ss} is a structural parameter that factors in changes in lattice parameter and shear modulus, and c is solute concentration, expressed in atomic fraction. The strengthening increment values predicted by Eq. (8) are listed and compared to the experimentally measured increment values, as shown in Table 4. The predicted and experimental strengthening increment values are within an order of magnitude of each other. Thus, we propose that changes in cation-dislocation interaction energies caused by changes in composition lead to solid-solution strengthening, which contributes to the observed changes in hardness of the single-phase samples as a function of composition.

In addition to the elastic effect described above, there is an additional chemical effect caused by changes in energy associated with cation-cation interactions, which correlate with changes in elastic modulus [41]. This energy depends on the crystallographic configuration (i.e., nearest neighbors). As the composition changes, crystallographic configurations change, causing bond lengths, and thus, bond energies, to change accordingly. The elastic modulus is strongly associated with bond energy, which can be approximated through bond length [42]. A longer bond length corresponds to a lower bond energy, and vice versa. In the case of a crystalline random solid solution such as the TM-ESO, the bond length can be approximated by lattice parameter. We used lattice parameters estimated by Rietveld refinement to analyze the changes in the room-temperature elastic modulus for the single-phase equimolar, Co-deficient, and Cu-deficient TM-ESO compositions, as listed in Table 5. The elastic modulus increases as the lattice parameter decreases, indicating that a chemical effect contributes to the changes in elastic modulus values as a function of composition observed for the single-phase samples.

Table 4

Predicted and experimental strengthening increment values for solid-solution strengthening of single-phase TM-ESOs. The increment values represent the change in hardness from the baseline equimolar composition.

TM-ESO Composition	Predicted Increment (MPa)	Experimental Increment (MPa)
Cu-deficient	−830	−1600
Co-deficient	410	610

Table 5

Room-temperature elastic modulus values and corresponding lattice parameters for single-phase equimolar, Co-deficient, and Cu-deficient TM-ESO.

TM-ESO Composition	Elastic Modulus (GPa)	Lattice Parameter (Å)
Equimolar	140	4.2326
Co-deficient	160	4.2312
Cu-deficient	170	4.2307

5.0. Conclusions

The influence of the entropic phase transformation on the room-temperature mechanical behavior of multiphase TM-ESOs was investigated. Single-phase equimolar samples were prepared through conventional sintering and were heat treated to form Cu-rich tenorite and Co-rich spinel secondary phases. Single-phase Co-deficient and Cu-deficient compositions were also prepared and heat treated to isolate the Cu-rich tenorite and Co-rich spinel secondary phases, respectively, and to study the influence of these secondary phases on mechanical behavior independent of one another. SEM, EDS, and XRD were used to characterize the secondary phase composition, morphology, and distribution in multiphase TM-ESO samples. STEM was used to study how dislocations interact with secondary phase particles inside and outside the deformation zone in multiphase equimolar TM-ESO. Hardness and elastic modulus were measured at room temperature with micro-indentation and nanoindentation, respectively. The key findings of this investigation are as follows:

1. Equimolar and Co-deficient samples experience an increase in room-temperature hardness after 2 h of heat treatment and a decrease in hardness after 12 h of heat treatment. This change in hardness is attributed to a switch in the operative strengthening mechanism from modulus hardening to Orowan hardening as the Cu-rich tenorite secondary phase particles grow and coarsen.
2. Cu-deficient samples experience a gradual increase in room-temperature hardness from 2 h to 12 h of heat treatment, due to a change in the operative strengthening mechanism from coherency hardening to modulus hardening. This change is attributed to the formation of Co-rich spinel secondary phase particles through the nucleation of nanoparticle precursor phases and eventual transformation into secondary phase particles.
3. The amount of secondary phase influences the room-temperature elastic modulus of TM-ESO, similar to conventional composite materials.
4. Changing the composition influences the room-temperature hardness and elastic modulus of single-phase TM-ESO due to changes in cation-dislocation and cation-cation interaction energies, respectively.

Overall, the entropic phase transformation, which controls the formation of secondary phases, influences the room-temperature mechanical behavior of TM-ESOs. The interactions between dislocations and secondary phase particles play a significant role in the hardness of TM-ESOs. Our analysis of hardness trends indicates that the mechanical behavior of single-phase and multiphase TM-ESO is influenced by solid-solution and precipitation strengthening mechanisms, respectively. Additionally, lattice parameter and cation configuration within the crystal structure influence the elastic modulus of single-phase and multiphase TM-ESOs, respectively. As the phase transformation of TM-ESOs is reversible, this study shows that the microstructure can be manipulated to tailor the mechanical behavior of TM-ESOs through simple heat treatment.

CRediT authorship contribution statement

Salma A. El-Azab: Writing – review & editing, Writing – original draft, Methodology, Investigation, Formal analysis, Data curation, Conceptualization. **Jacob E. Norman:** Writing – review & editing, Data curation. **Luz Gomez:** Data curation. **Alexander D. Dupuy:** Writing – review & editing, Supervision, Funding acquisition, Conceptualization. **Julie M. Schoenung:** Writing – review & editing, Supervision, Resources, Project administration, Funding acquisition.

Declaration of competing interest

The authors declare that they have no known competing financial interests or personal relationships that could have appeared to influence the work reported in this paper.

Acknowledgements

The authors are grateful for support from the National Science Foundation (NSF) under award CMMI-2029966 and CMMI-2414950. SAE is thankful for support from NSF award DGE-1839285, the ARCS Foundation, and the University of California, Irvine (UC Irvine) Provost Ph.D. Fellowship. The authors acknowledge the use of facilities and instrumentation at the UC Irvine Materials Research Institute (IMRI), which is supported in part by NSF through the UC Irvine Materials Research Science and Engineering Center (DMR-2011967). The authors also acknowledge the use of facilities at the Advanced Casting Research Center at UC Irvine. The authors thank Dr. Xin Wang, Dr. Katherine Acord, Brandon Fields, and Sakshi Bajpai for their experimental and analytical assistance.

Supplementary materials

Supplementary material associated with this article can be found, in the online version, at doi:10.1016/j.actamat.2024.120428.

References

[1] D.B. Miracle, High entropy alloys as a bold step forward in alloy development, Nat. Commun. 10 (1) (2019) 1805, https://doi.org/10.1038/s41467-019-09700-1. Dec.

[2] B. Cantor, I.T.H. Chang, P. Knight, A.J.B. Vincent, Microstructural development in equiatomic multicomponent alloys, Mater. Sci. Eng. A 375–377 (2004) 213–218, https://doi.org/10.1016/j.msea.2003.10.257. Jul.

[3] J.-W. Yeh, S.-K. Chen, S.-J. Lin, J.-Y. Gan, T.-S. Chin, T.-T. Shun, C.-H. Tsau, S.-Y. Chang, Nanostructured high-entropy alloys with multiple principal elements: novel alloy design concepts and outcomes, Adv. Eng. Mater. 6 (5) (2004) 299–303, https://doi.org/10.1002/adem.200300567. May.

[4] C.M. Rost, E. Sachet, T. Borman, A. Moballegh, E.C. Dickey, D. Hou, J.L. Jones, S. Curtarolo, J.-P. Maria, Entropy-stabilized oxides, Nat. Commun. 6 (1) (2015) 8485, https://doi.org/10.1038/ncomms9485. Dec.

[5] A.D. Dupuy, X. Wang, J.M. Schoenung, Entropic phase transformation in nanocrystalline high entropy oxides, Mater. Res. Lett. 7 (2) (2019) 60–67, https://doi.org/10.1080/21663831.2018.1554605. Feb.

[6] T. Runčevski, C.M. Brown, The Rietveld refinement method: half of a century anniversary, Cryst. Growth Des. 21 (9) (2021) 4821–4822, https://doi.org/10.1021/acs.cgd.1c00854. Sep.

[7] A.D. Dupuy, M.R. Chellali, H. Hahn, J.M. Schoenung, Nucleation and growth behavior of multicomponent secondary phases in entropy-stabilized oxides, J. Mater. Res. 38 (1) (2023) 198–214, https://doi.org/10.1557/s43578-022-00784-y. Jan.

[8] J.L. Braun, C.M. Rost, M. Lim, A. Giri, D.H. Olson, G.N. Kotsonis, G. Stan, D. W. Brenner, J.-P. Maria, P.E. Hopkins, Charge-Induced disorder controls the thermal conductivity of entropy-stabilized oxides, Adv. Mater. 30 (2018) 1805004, https://doi.org/10.1002/adma.201805004.

[9] K.C. Pitike, A.E. Marquez-Rossy, A. Flores-Betancourt, D.X. Chen, K. Santosh, V. R. Cooper, E. Lara-Curzio, On the elastic anisotropy of the entropy-stabilized oxide (Mg, Co, Ni, Cu, Zn)O compound, J. Appl. Phys. 128 (1) (2020) 015101, https://doi.org/10.1063/5.0011352. Jul.

[10] W. Hong, F. Chen, Q. Shen, Y. Han, W.G. Fahrenholtz, L. Zhang, Microstructural evolution and mechanical properties of (Mg,Co,Ni,Cu,Zn)O high-entropy ceramics, J. Am. Ceram. Soc. (2018) jace.16075, https://doi.org/10.1111/jace.16075. Oct.

[11] X. Wang, J. Cortez, A.D. Dupuy, J.M. Schoenung, W.J. Bowman, High entropy oxide (Co,Cu,Mg,Ni,Zn)O exhibits grain size dependent room temperature deformation, Mater. Res. Lett. 11 (3) (2023) 196–204, https://doi.org/10.1080/21663831.2022.2135409. Mar.

[12] P.H. Mayrhofer, A. Hörling, L. Karlsson, J. Sjölén, T. Larsson, C. Mitterer, L. Hultman, Self-organized nanostructures in the Ti–Al–N system, Appl. Phys. Lett. 83 (10) (2003) 2049–2051, https://doi.org/10.1063/1.1608464. Sep.

[13] T. Sakuma, Y.-I. Yoshizawa, and H. Suto, “The modulated structure formed by isothermal ageing in Zr02-5.2 moi % Y20a alloy,” p. 8.

[14] Y. Zhong, W. Xiang, L. He, J. Li, J. Hao, Z. Tian, X. Wang, Directionally solidified Al2O3/(Y0.2Er0.2Yb0.2Ho0.2Lu0.2)3Al5O12 eutectic high-entropy oxide ceramics with well-oriented structure, high hardness, and low thermal conductivity, J. Eur. Ceram. Soc. 41 (14) (2021) 7119–7129, https://doi.org/10.1016/j.jeurceramsoc.2021.07.049. Nov.

[15] Y. Zhong, Z. Li, X. Wang, Seed-crystal-induced directional solidification toward Al2O3/(Y0.2Er0.2Yb0.2Ho0.2Lu0.2)3Al5O12/ZrO2 ternary eutectic ceramics, Acta Mater 262 (2024) 119369, https://doi.org/10.1016/j.actamat.2023.119369. Jan.

[16] T.-Z. Tu, J.-X. Liu, Y. Wu, L. Zhou, Y. Liang, G.-J. Zhang, Synergistic effects of high-entropy engineering and particulate toughening on the properties of rare-earth aluminate-based ceramic composites, J. Adv. Ceram. 12 (4) (2023) 861–872, https://doi.org/10.26599/JAC.2023.9220726. Apr.

[17] Y. Feng, X. Liu, P. Zhang, Y. Han, S. Zhai, W. Pan, C. Wan, Dendrite microstructure formation and enhanced toughness in high-entropy REAlO$_3$–RE$_2$Zr$_2$O$_7$ eutectic oxide, J. Am. Ceram. Soc. 106 (12) (2023) 7736–7744, https://doi.org/10.1111/jace.19379. Dec.

[18] A.D. Dupuy, J.M. Schoenung, Morphological evolution in nanostructured secondary phases in entropy stabilized oxides, Mater. Charact. 193 (2022) 112301, https://doi.org/10.1016/j.matchar.2022.112301. Nov.

[19] S.H. Gould, The method of archimedes, Am. Math. Mon. 62 (7P1) (1955) 473–476, https://doi.org/10.1080/00029890.1955.11988664. Aug.

[20] D.M.D. Abràmoff, Image processing with ImageJ, Biophotonics Int (2004) 7. Jul.

[21] A.I. Saville, A. Creuziger, E.B. Mitchell, S.C. Vogel, J.T. Benzing, J. Klemm-Toole, K.D. Clarke, A.J. Clarke, MAUD Rietveld refinement software for neutron diffraction texture studies of single- and dual-phase materials, Integrating Mater. Manuf. Innov. 10 (3) (2021) 461–487, https://doi.org/10.1007/s40192-021-00224-5. Sep.

[22] X. Li, B. Bhushan, A review of nanoindentation continuous stiffness measurement technique and its applications, Mater. Charact. 48 (1) (2002) 11–36, https://doi.org/10.1016/S1044-5803(02)00192-4. Feb.

[23] M. Mata, O. Casals, J. Alcalá, The plastic zone size in indentation experiments: the analogy with the expansion of a spherical cavity, Int. J. Solids Struct. 43 (20) (2006) 5994–6013, https://doi.org/10.1016/j.ijsolstr.2005.07.002. Oct.

[24] V.M. Matyunin, N. Abusaif, A.Y. Marchenkov, Characteristics of the deformed zone around Vickers indentations in metals, IOP Conf. Ser. Mater. Sci. Eng. 537 (3) (2019) 032004, https://doi.org/10.1088/1757-899X/537/3/032004. May.

[25] T.E. Mitchell, K.P.D. Lagerlöf, A.H. Heuer, Dislocations in ceramics, Mater. Sci. Technol. 1 (11) (1985) 944–949, https://doi.org/10.1179/mst.1985.1.11.944. Nov.

[26] Y. Han, X. Liu, Q. Zhang, M. Huang, Y. Li, W. Pan, P. Zong, L. Li, Z. Yang, Y. Feng, P. Zhang, C. Wan, Ultra-dense dislocations stabilized in high entropy oxide ceramics, Nat. Commun. 13 (1) (2022) 2871, https://doi.org/10.1038/s41467-022-30260-4. May.

[27] H. Vahidi, A.D. Dupuy, B.X. Lam, J. Cortez, P. Garg, T.J. Rupert, J.M. Schoenung, W.J. Bowman, Reversible enhancement of electronic conduction caused by phase transformation and interfacial segregation in an entropy-stabilized oxide, Adv. Funct. Mater. 34 (25) (2024) 2315895, https://doi.org/10.1002/adfm.202315895. Jun.

[28] T.H. Courtney, Mechanical Behavior of Materials, Waveland Press, 2005. Incorporated.

[29] G.K. Bansal, A.H. Heuer, Precipitation strengthening in non-stoichiometric Mg-Al spinel, in: R.C. Bradt, D.P.H. Hasselman, F.F. Lange (Eds.), Fracture Mechanics of Ceramics, Springer US, Boston, MA, 1974, pp. 677–690, https://doi.org/10.1007/978-1-4615-7014-1_15.

[30] Q. Wang, Z. Li, S. Pang, X. Li, C. Dong, P. Liaw, Coherent precipitation and strengthening in compositionally complex alloys: a review, Entropy 20 (11) (2018) 878, https://doi.org/10.3390/e20110878. Nov.

[31] K. Ma, H. Wen, T. Hu, T.D. Topping, D. Isheim, D.N. Seidman, E.J. Lavernia, J. M. Schoenung, Mechanical behavior and strengthening mechanisms in ultrafine grain precipitation-strengthened aluminum alloy, Acta Mater. 62 (2014) 141–155, https://doi.org/10.1016/j.actamat.2013.09.042. Jan.

[32] P.L. Meena, R. Kumar, K. Sreenivas, Structural, elastic and magnetic properties of spinel Co3O4, Indian J. Pure Appl. Phys. 56 (2018) 890–895.

[33] A. Kelly, R.B. Nicholson, Strengthening methods in crystals, Composites (1971) 10, https://doi.org/10.1016/0010-4361(71)90159-5.

[34] J.M. Silcock, T.J. Heal, H.K. Hardy, Structural ageing characteristics of binary aluminium-copper alloys, J. Inst. Met. 82 (1954) 239.

[35] D.A. Porter, K.E. Easterling, M.Y. Sherif, Phase Transformations in Metals and Alloys, 3rd ed., Taylor & Francis Group, Boca Raton, FL, 2009.

[36] L.J. Cohen, O. Ishai, The elastic properties of three-phase composites, J. Compos. Mater. 1 (4) (1967) 390–403, https://doi.org/10.1177/002199836700100407. Oct.

[37] X. Huang, G. Xie, X. Liu, H. Fu, L. Shao, Z. Hao, The influence of precipitation transformation on Young’s modulus and strengthening mechanism of a Cu–Be binary alloy, Mater. Sci. Eng. A 772 (2020) 138592, https://doi.org/10.1016/j.msea.2019.138592. Jan.

[38] M. Meyers, K. Chawla, Mechanical Behavior of Materials, 2nd ed., Cambridge University Press, 2008.

[39] R. Chaim, Percolative composite model for prediction of the properties of nanocrystalline materials, J. Mater. Res. 12 (7) (1997) 1828–1836, https://doi.org/10.1557/JMR.1997.0251. Jul.

[40] G. Bracq, M. Laurent-Brocq, C. Varvenne, L. Perrière, W.A. Curtin, J.-M. Joubert, I. Guillot, Combining experiments and modeling to explore the solid solution strengthening of high and medium entropy alloys, Acta Mater. 177 (2019) 266–279, https://doi.org/10.1016/j.actamat.2019.06.050. Sep.

[41] S. Nag, W.A. Curtin, Effect of solute-solute interactions on strengthening of random alloys from dilute to high entropy alloys, Acta Mater. 200 (2020) 659–673, https://doi.org/10.1016/j.actamat.2020.08.011. Nov.

[42] E. Isotta, W. Peng, A. Balodhi, A. Zevalkink, Elastic moduli: a tool for understanding chemical bonding and thermal transport in thermoelectric materials, Angew. Chem. Int. Ed. 62 (12) (2023) e202213649, https://doi.org/10.1002/anie.202213649. Mar.